TITLE:

Numerical simulations for describing generation of excavation damaged zone: Important case study at Horonobe underground research laboratory

AUTHOR(S):

Ogata, Sho; Yasuhara, Hideaki

CITATION:

Ogata, Sho ...[et al]. Numerical simulations for describing generation of excavation damaged zone: Important case study at Horonobe underground research laboratory. Rock Mechanics Bulletin 2023, 2(3): 100063.

ISSUE DATE:

2023-07

URL:

http://hdl.handle.net/2433/284578

RIGHT:

© 2023 Chinese Society for Rock Mechanics & Engineering. Publishing services by Elsevier B.V. on behalf of KeAi Co. Ltd.; This is an Open Access article under the CC BY-NC-ND 4.0 license.

京都大学学術情報リポジトリ
KURENAI 紅
Kyoto University Research Information Repository

京都大学 KYOTO UNIVERSITY
A Self-archived copy in
Kyoto University Research Information Repository
https://repository.kulib.kyoto-u.ac.jp
京都大学学術情報リポジトリ KURENAI 紅 Kyoto University Research Information Repository

Rock Mechanics Bulletin 2 (2023) 100063

Contents lists available at ScienceDirect

Rock Mechanics Bulletin

journal homepage: www.keaipublishing.com/en/journals/rock-mechanics-bulletin

Numerical simulations for describing generation of excavation damaged zone: Important case study at Horonobe underground research laboratory

Sho Ogata [a,*], Hideaki Yasuhara [b]

[a] Osaka University, Suita, 565-0871, Japan
[b] Kyoto University, Kyoto, 615-8540, Japan

ARTICLE INFO

Keywords:
Generation of rock fracture
Excavation damaged zone
Mudstone
Horonobe underground research laboratory
Damage model

ABSTRACT

The aim of the present research was to establish a case study for the prediction of the unknown EDZ (Excavation Damaged Zone) distribution using a numerical analysis calibrated by replicating the trends in the EDZ observed from one of the representative underground research fields in Japan (Horonobe URL). In this study, a 2D numerical analysis using a damage model, which can determine rock deformation and fracturing simultaneously, is presented. It was calibrated to reproduce the excavation of the gallery at the Horonobe URL at a depth of 350 m. Simulated results show an excellent agreement with the extent of the measured EDZ and capture the failure modes of EDZ fractures suggested by the in-situ observations. Finally, the calibrated numerical analysis was used to realistically estimate the EDZ formation for the geological disposal of high-level radioactive waste (HLW) under the same environment as that of the above-mentioned galley at the Horonobe URL. Consequently, it was shown that the tensile/shear hybrid fractures dominantly constituted the EDZ and propagated to a maximum extent of about 0.3 m from the cavity wall during the cavity excavation for the HLW disposal. Overall, the calibrated numerical analysis and resulting estimations, targeted for the environment at the depth of 350 m at the Horonobe URL, where mudstone is located, should be useful for predicting the trends in the EDZ distribution expected in the implementation of HLW disposal projects under deep geological conditions, such as those that exist in Japan, which are dominated by sedimentary rocks, including mudstone.

1. Introduction

To ensure the performance of geological disposal facilities for high-level radioactive waste (HLW), the spatial distribution of the hydraulic and mechanical properties within a rock mass, which plays the important role of a natural barrier, should be evaluated (Japan Nuclear Cycle Development Institute, 2000). To achieve this, it is essential to adequately predict the distribution of the Excavation Damaged Zone (EDZ), which is formed by the initiation and propagation of multiple fractures during the excavation of a disposal cavity for radioactive waste. This is because such a zone is expected to cause an increase in permeability and a decrease in the stiffness and strength of the rock mass surrounding the excavated cavity (Kelsall et al., 1984; Japan Nuclear Cycle Development Institute, 2000; Souley et al., 2001; Tsang et al., 2005; Zhang, 2016; Aoyagi and Ishii, 2018). In particular, in order to predict the detailed distribution of the unknown EDZ, a numerical simulation should be an effective method.

In order to achieve the most reliable prediction of the unknown EDZ distribution, it is necessary to apply a calibrated analysis model (e.g. finite element model) when implementing projects for the geological disposal of HLW under specific underground conditions, by reproducing the trends in the EDZ observed in pre-in-situ tests conducted under the same or similar underground conditions. In view of this, it would be beneficial to gather and present examples from around the world of the implementation of EDZ predictions with model calibrations by targeting some well-known representative underground conditions that have been intensively studied.

Within this context, a number of attempts have been made to numerically reproduce the characteristics of the EDZ in in-situ excavation tests conducted at several underground research laboratories (URLs) (e.g., Hajiabdolmajid et al., 2002; Jia et al., 2012; Li and Liu, 2013; Li and Tang, 2015; Giger et al., 2015; Vlachopoulos and Vazaios, 2018; Aoyagi and Ishii, 2018). On the other hand, one of the URLs, where only very limited attempts have been made to simulate the distribution of the EDZ by a numerical analysis, is the Horonobe URL in Japan. Several in-situ excavation tests have been conducted at this site along with

* Corresponding author.
E-mail address: ogata@civil.eng.osaka-u.ac.jp (S. Ogata).

https://doi.org/10.1016/j.rockmb.2023.100063
Received 28 February 2023; Received in revised form 28 June 2023; Accepted 29 June 2023
Available online 29 June 2023
2773-2304/© 2023 Chinese Society for Rock Mechanics & Engineering. Publishing services by Elsevier B.V. on behalf of KeAi Co. Ltd. This is an open access article under the CC BY-NC-ND license (http://creativecommons.org/licenses/by-nc-nd/4.0/).

京都大学 KYOTO UNIVERSITY
A Self-archived copy in
Kyoto University Research Information Repository
https://repository.kulib.kyoto-u.ac.jp
京都大学学術情報リポジトリ KURENAI 紅 Kyoto University Research Information Repository

observations of the EDZ under the deep geological environment composed of mudstone. Since crystalline and sedimentary rocks account for a large proportion of the deep underground geological environment in Japan, abundant data on the physical and chemical properties of these representative rock types have been collected from URLs by the Japan Atomic Energy Agency (JAEA) (e.g., Saegusa et al., 2007; Ota et al., 2007). Specifically, research works, such as in-situ and laboratory experiments on crystalline rock (granite), have been conducted at the Mizunami URL in Gifu Prefecture, Japan, and on sedimentary rock (mudstone) at the Horonobe URL in Hokkaido, Japan. Thus, the advancement of the numerical analysis, by simulating the experimental works at these two URLs, is of great importance for the success of projects for the geological disposal of HLW in Japan. From this perspective, it is necessary to address the lack of numerical studies with respect to the EDZ generated in the mudstone at the Horonobe URL.

To date, the only numerical study that has attempted to simulate the observed EDZ in the Horonobe URL is that by Aoyagi and Ishii (2018). In their study, the simulated results roughly capture the extent of the actual EDZ detected by in-situ tests, but they do not represent the heterogeneous distributions of the generated fractures that form the EDZ, which may be important for reasonably describing the inhomogeneous damage-induced hydraulic and mechanical behavior within the excavated rock mass. On the other hand, in Ogata et al. (2020), the authors performed an excavation analysis, under the subsurface conditions assumed for the Horonobe area of Hokkaido, by employing a continuous damage model that can represent the heterogeneous fracture generation based on the approach proposed by Tang (1997) and Zhu and Tang (2004). However, this excavation analysis was not calibrated through a comparison with the results of in-situ excavation tests in the Horonobe area (e.g., Horonobe URL), and thus, would need to be further improved in order to capture the actual characteristics of the EDZ as realistically as possible. For example, in our excavation analysis (Ogata et al., 2020), the total stress components are used in the failure criteria to determine the crack initiation, although there is a suggestion that the effective stress components, considering the pore pressure under the assumption of undrained conditions, should be used in the failure criteria. This is because tension-induced fracturing may occur in a very short time during the gallery excavation (Blümling et al., 2007). In addition, not only in our excavation analysis (Ogata et al., 2020), but also in most numerical analyses dealing with rock fracture generation (e.g., Li et al., 2013; Li and Tang, 2015; Jia et al., 2012; Wang et al., 2016; Marschall et al., 2017; Vlachopoulos and Vazaios, 2018), rock deformation and fracture generation, which do in fact affect each other in parallel, are not solved simultaneously and do not affect each other within a single computational step (e.g., a time step, a loading step, a sub-loading step, etc.). This conventional approach may lead to many deviations from the actual mechanical responses of the rocks due to the occurrence of time lags with respect to the interaction between rock deformation and fracture generation. In the numerical analyses mentioned above, for which the tight coupling between rock deformation and fracture generation is not solved, the process for determining the nucleation and growth of fractures is performed separately after the completion of the stress/deformation analysis (i.e., mechanical equilibrium analysis). Then, the updated information on the fractures is reflected in the stress/deformation analysis at the next computational step, not within the current computational step. In other words, the effect of the nucleation and growth of fractures on the deformation is reflected across the computational steps.

The aim of the present study is to establish a case study for the numerical prediction of the unknown EDZ distribution, due to the rock fracturing process, using an analysis model calibrated by reproducing the characteristics of the EDZ, observed at one of the representative underground research fields in Japan (Horonobe URL), in order to contribute to safety assessments of the natural barrier in the implementation of projects for the geological disposal of HLW in Japan.

In this study, a 2D numerical analysis is presented. It is based on the finite element method (FEM) with the continuous damage model, which includes the fully coupled computation of rock deformation and fracture generation and considers the pore pressure effect. Then, it is applied to a numerical analysis of the excavation of the gallery of the Horonobe URL at a depth of 350 m (Aoyagi and Ishii, 2018), and calibrated to follow the observed results from in-situ tests for the characteristics of the EDZ distribution in the mudstone (e.g., the extent of the EDZ and the failure modes of the generated fractures). Finally, the calibrated analysis model is used as a case study to predict the unknown EDZ distribution in the geological disposal of HLW under the same geological environment as that of the above-mentioned Horonobe URL gallery excavation.

2. Governing equations

The numerical analysis in this work, which is capable of describing the distributions of stress/deformation, and the fracture generation within rock masses, is implemented with the FEM engine of COMSOL MULTIPHYSICS (COMSOL, 2021). The characteristic feature of the proposed numerical analysis lies in its ability to clarify both rock deformation and fracturing simultaneously in the calculation of the mechanical balance for accurately tracking the transition of the mechanical responses during the ongoing EDZ expansion within a rock mass. Basically, both the fracture generation law induced by stress or strain (e.g., failure criteria and law of damage evolution) and the constitutive law (stress-strain relation), including the influence of fracturing (e.g., damage model), can be written down in terms of displacement as an unknown variable. Therefore, substituting the equations for the fracture generation law and constitutive law into the mechanical equilibrium equation yields the governing equation with displacement as the only unknown variable. By solving this governing equation, based on the FEM in the proposed numerical analysis, both fracturing and deformation are naturally solved simultaneously and affect each other in parallel within the current simulation step (i.e., full coupling). On the other hand, in most of the previous numerical studies that have discussed the generation of rock fractures (e.g., Li et al., 2013; Li and Tang, 2015; Jia et al., 2012; Wang et al., 2016; Marschall et al., 2017; Vlachopoulos and Vazaios, 2018), fracturing and deformation were not reported to influence each other within a single computational step (e.g., a time step, a loading step, a sub-loading step, etc.). Specifically, in the above numerical studies, "after" the mechanical equilibrium analysis has been fully completed, judgement of the cracking for each finite element is implemented from the already computed stress/strain values. Then, the updated failure condition is reflected in the mechanical equilibrium analysis at the "next" computational step, not at the "current" computational step.

In the following, the governing equations solved by the numerical analysis are introduced.

(a) Mechanical equilibrium

In the present study, assuming the plane strain condition, the distributions of stress/deformation within the rock are described by solving the quasi-static equilibrium equation and the constitutive relation between stress and strain, taking account of the damage evolution and pore pressure, as follows:

$$\nabla \cdot \boldsymbol{\sigma} + \boldsymbol{b} = 0 \quad \text{and} \quad \boldsymbol{\varepsilon} = \frac{1}{2}\left[\nabla \boldsymbol{u} + (\nabla \boldsymbol{u})^{\mathrm{T}}\right], \tag{1}$$

$$\boldsymbol{\sigma} = (1 - D)\boldsymbol{C} : \boldsymbol{\varepsilon} + \alpha_B p \boldsymbol{I}, \tag{2}$$

where $\boldsymbol{\sigma}$ [Pa] is the stress tensor, $\boldsymbol{b}$ [Pa m^{-1}] is the body force, $\boldsymbol{C}$ [Pa] is the elasticity tensor, $\boldsymbol{\varepsilon}$ [−] is the strain tensor, $\boldsymbol{u}$ [m] is the displacement vector, p [Pa] is the pore pressure, $\boldsymbol{\varepsilon}$ [−] is the strain tensor, D[-] is the scalar damage variable that varies from 0 to D_{cri} (= 0.98) and represents the degree of damage to the target media, α_B [−] is the Biot-Willis coefficient, and I [-] is the identity tensor. D is 0 when damage does not occur and D_{cri} when complete damage occurs. It should be noted that

京都大学 KYOTO UNIVERSITY
A Self-archived copy in
Kyoto University Research Information Repository
https://repository.kulib.kyoto-u.ac.jp
京都大学学術情報リポジトリ KURENAI 紅 Kyoto University Research Information Repository

when D reaches 1.0, the damaged elasticity tensor (1-D) $\boldsymbol{C}$ is zero, which would cause instability in finite element analysis. Thus, to prevent this, the damage limit D_{cri} is set slightly less than 1.0. In this study, compressive stress is set to be positive, while tensile stress is set to be negative.

(b) Damage evolution

The fracture generation process within a rock mass is calculated by utilizing an isotropic damage model, assuming continuum media that do not represent the explicit fracture, by inserting discontinuous surfaces into the computational domain, etc. In this damage model, assuming that microscopic ~ mesoscopic cracking occurs isotropically within each finite element, to the extent that it satisfies the failure criteria, the material stiffness of the elements is degraded according to the degree of damage due to cracking expressed by the damage variable D. In other words, a damaged element for which the failure criteria ($D > 0$) have been satisfied, is a cracked element, while a completely damaged element ($D = D_{cri}$) is a fully cracked element. As is commonly used in numerical analyses employing the above-mentioned isotropic damage model (e.g., Zhu and Tang, 2004; Li and Tang, 2015), the areas where cracked elements are coalescing represent the approximate fracture zones. In this work, damage induced by tension and shear is determined based on the failure criteria, considering the maximum tensile stress criterion and the Mohr-Coulomb failure criterion addressed in Tang (1997), Zhu and Tang (2004), and Li and Tang (2015), and expressed by

$$\begin{cases} F_t = \kappa_t^{\max} - f_{t0} \\ F_s = \kappa_s^{\max} - f_{c0} \end{cases} \tag{3}$$

$$\kappa_t = -\sigma_3 \tag{4}$$

$$\kappa_s = \sigma_1 - \frac{1+\sin\theta}{1-\sin\theta}\sigma_3 \tag{5}$$

where F_t and F_s are the two damage threshold functions for tensile damage and shear damage, respectively, $\kappa_t^{\max}$ and $\kappa_s^{\max}$ are the maximum values of κ_t and κ_s, respectively, from the beginning of the numerical analysis to the current computational step, κ_t and κ_s are variables for storing the driving forces of the tension damage and shear damage, respectively, σ_1 [Pa] and σ_3 [Pa] are the maximum and minimum principal stresses, respectively, f_{t0} [Pa] and f_{c0} [Pa] are the uniaxial tensile strength and uniaxial compressive strength, respectively, and θ [°] is the internal friction angle. Based on the linear elastic law, the principal stresses in Eqs. (4) and (5) are calculated by the principal strain and volumetric strain, as follows:

$$\sigma_i = \frac{E}{1+\nu}\left[\varepsilon_i + \frac{\nu}{1-2\nu}\varepsilon_v\right] \tag{6}$$

where ε_i ($i = 1, 2, 3$) are the principle strains in the first, second, and third principal stress directions, respectively, ε_v [−] is the volumetric strain, and ν [−] is Poisson's ratio.

According to the failure criteria of Eq. (3), damage by each failure mode is computed with reference to Smith and Young (1955), as follows:

$$\begin{cases} D_t = D_s = 0 & F_t < 0 \text{ and } F_s < 0 \\ D_t = 1 - \exp\left(1 - \dfrac{\kappa_t^{\max}}{\eta f_{t0}}\right) & F_t \geq 0 \\ D_s = 1 - \exp\left(1 - \dfrac{\kappa_s^{\max}}{\eta f_{c0}}\right) & F_s \geq 0 \end{cases} \tag{7}$$

where D_t [−] is the tension-induced damage, D_s [−] is the shear-induced damage, and η [−] is the residual strength constant. It should be noted that the maximum values for the driving components of tension damage and shear damage are used for the failure criteria and damage evolution law (Eqs. (3) and (7)). This is because the recovery of the degrees of damage due to unloading, etc., is not considered in this study. Thus, damage variable D is expressed by considering both tensile damage and shear damage in the same way as it is in Fukuda et al. (2019), as

$$D = \min\left(D_{cri}, \sqrt{D_t^2 + D_s^2}\right) \tag{8}$$

It should be noted that, in the numerical analysis of the current work, Eq. (1) is solved by substituting Eqs. (2) and (8) with only the displacement as the unknown variable. This means monotonically full coupling computation with respect to rock deformation and rock fracturing within a target media.

(c) Heterogeneity of mechanical properties

When considering the heterogeneity of a rock mass, the local mechanical properties within the rock mass (i.e., mechanical properties of all the individual finite elements in the calculation domains), are defined in the current study by statistical dispersion based on the Weibull distribution (Weibull, 1951). Among the mechanical properties, the elastic modulus, uniaxial tensile strength, and uniaxial compressive strength are set by the following probability density function (Tang, 1997; Zhu and Tang, 2004):

$$f(\xi) = \frac{m}{\xi^s}\left(\frac{\xi}{\xi^s}\right)^{m-1}\exp\left[-\left(\frac{\xi}{\xi^s}\right)^m\right], \tag{9}$$

where ξ is the mechanical parameter of each finite element in the calculation domain, such as the strength and elastic modulus (i.e., $\xi = E_0$, f_{t0}, and f_{c0}), ξ^s is the characteristic value for the distribution of the mechanical parameters, ξ (i.e., $\xi^s = E_0^s$, f_{t0}^s, and f_{c0}^s), and m [−] is the homogeneity index for the material properties which describe the shape of the distribution function. To obtain the spatial distributions of the values for the mechanical parameters according to the Weibull statistical function, a set of random numbers ψ in the range 0–1.0 is created and assigned to each finite element. Then, the mechanical parameter ξ_i of each finite element can be defined, as follows:

$$\xi_i = \xi^s \ln\left(\frac{1}{1-\psi_i}\right)^{\frac{1}{m}} \tag{10}$$

3. Calibration of numerical analysis

Among the excavation works within the horizontal gallery at a depth of 350 m in the Horonobe URL (Fig. 1), the excavation in Niche No. 3 (Fig. 2), presented in Aoyagi and Ishii (2018), was selected for the calibration of the proposed numerical analysis. In this calibration, the consistency between the simulated results and the fundamental characteristics of the EDZ in the mudstone formation (extent of the EDZ and failure mode of generated fractures) observed from the in-situ tests, is examined.

3.1. Set up of simulation

The cross section of Niche No. 3 (horseshoe-shaped niche), which has a width of 4.0 m (i.e., niche diameter d is 4.0 m), a height of 3.2 m, and a length of 25 m, is shown in Fig. 3. This niche is mainly supported by 200-mm-thick shotcrete, 2.0-m-long rockbolts, and steel arch ribs. During the excavation, the support structures were installed every 1.0 m with the progression of the excavation face for the first 5.0-m section from the entrance of the niche, and thereafter, every 1.5 m for the last 5.0-m section to the end of the niche. No rockbolts were inserted in the last 10-m section of the niche.

The model geometry and boundary conditions, simulating the above-introduced in-situ excavation by the 2D numerical analysis, are shown in

京都大学 KYOTO UNIVERSITY
A Self-archived copy in
Kyoto University Research Information Repository
https://repository.kulib.kyoto-u.ac.jp
京都大学学術情報リポジトリ KURENAI 紅 Kyoto University Research Information Repository

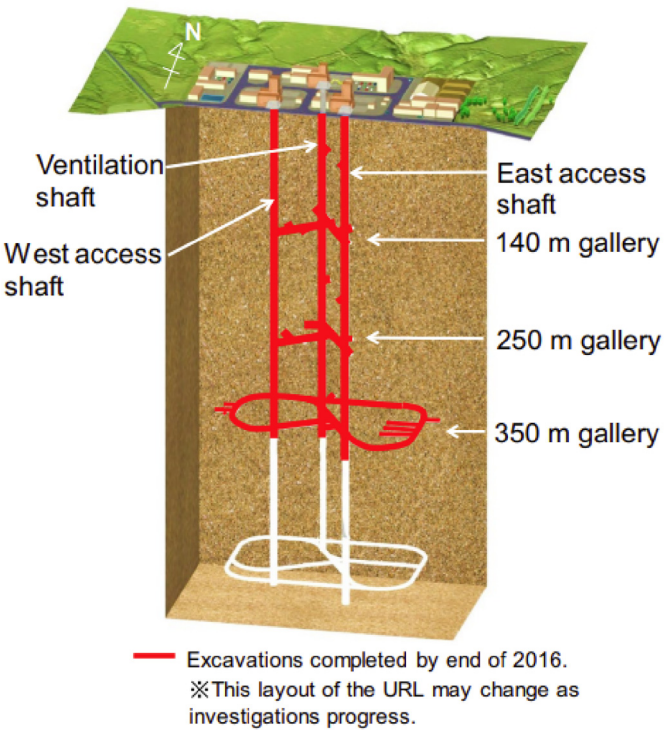

Fig. 1. Layout of Horonobe URL (after Aoyagi and Ishii (2018)).

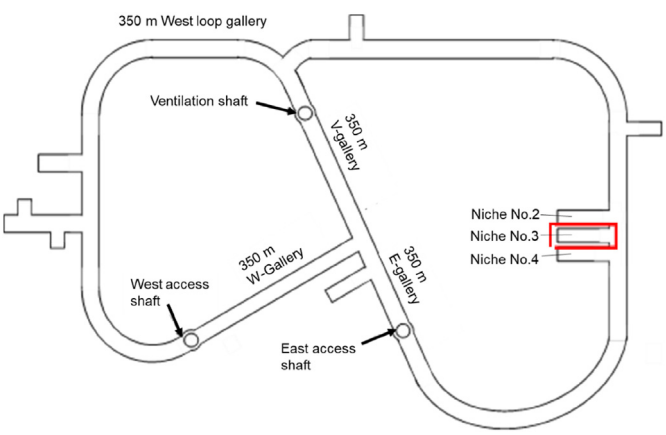

Fig. 2. Layout of gallery at depth of 350 m (after Aoyagi and Ishii (2018)).

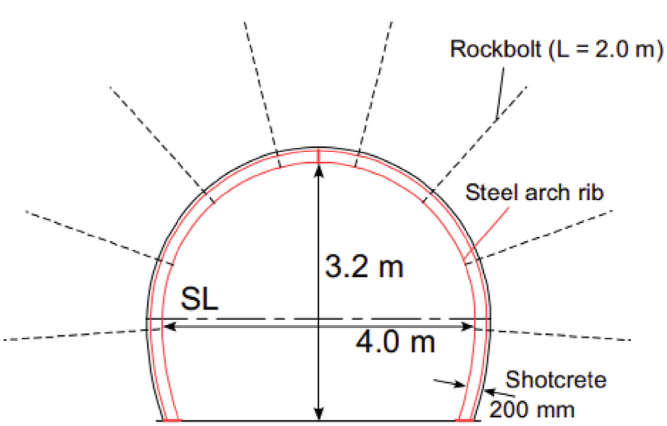

Fig. 3. Vertical cross section (after Aoyagi and Ishii (2018)).

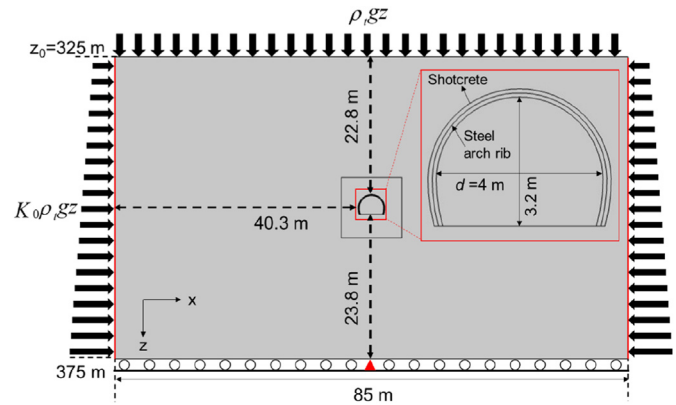

Fig. 4. Description of numerical analysis for simulating excavation of Niche No. 3.

Fig. 4. With respect to the size of the numerical domain, by referring to the literature that includes the desirable domain setting of the FEM for tunnel excavations (Tamura and Adachi, 2002; Tomita et al., 2010), the distances from the wall of the niche to the upper and lower edges within the numerical domain were set to be roughly equivalent to 5 d (upper: 22.8 m and lower: 23.8 m), respectively, while the distance to the lateral edges was set to be roughly equivalent to 10 d (40.3 m). The numerical domain was discretized into 502800 rectangular elements. In the 10-m-square area around the niche where it is expected that all possible fracture generation areas can be adequately covered, the mesh size was set to be much finer than in other areas in order to reasonably reduce the computational costs (Fig. 5). Notably, in general, due to the nature of the continuous damage model with spatially heterogeneous mechanical properties used in this study, the smaller the mesh size becomes, the closer the fractured zones can be drawn to the actual localized heterogeneous distribution. Unfortunately, trial FEM calculations for this excavation analysis revealed that setting a mesh size smaller than about 0.02 m for a 10-m-square area around the cavity would require an enormous amount of computation time. Based on these findings, the average mesh size of the 10-m-square area around the niche was set to approximately 0.02 m. Setting up a smaller size mesh (e.g., <0.01 m) would require massively parallel computations, which is an issue for the future. In addition, the average mesh size of the area outside of the 10-m square around the niche was set to about 0.8 m.

Since the pore pressure at 350 m depth prior to the excavation of was ca. 3.5 MPa based on pore pressure measurement in the boreholes.

In terms of the initial stress conditions, the minimum principal stress (σ_x = 5.49 MPa) and vertical stress (σ_z = 5.61 MPa) at 350 m depth on the target site, were estimated on the bases of the hydraulic fracturing tests conducted in the boreholes around the Horonobe URL drilled prior to the excavation (surface-based investigation) and in the 350 m gallery (Aoyagi et al., 2013). Besides, based on pore pressure measurement in the boreholes, the pore pressure at 350 m depth prior to the excavation was ca. 3.5 MPa and is clearly proportional to depth. Notably, in this analysis, the initial stress components except at 350 m was given assuming that the initial stress is also proportional to depth as is the pore water pressure. Specifically, the minimum principal stress σ_x and vertical stress σ_z for applying to top and side boundaries of numerical domain, were calculated by the following equations referring to measured stress values at 350 m depth.

$$\sigma_x = K_0 \rho_t g z \tag{11}$$

$$\sigma_z = \rho_t g z \tag{12}$$

where ρ_t is the nominal density obtained so that Eq. (12) equals the measured value of 5.61 MPa at 350 m depth, K_0 is the lateral pressure coefficient calculated from the ratio of minimum principal stress (5.49

京都大学 KYOTO UNIVERSITY
A Self-archived copy in
Kyoto University Research Information Repository
https://repository.kulib.kyoto-u.ac.jp
京都大学学術情報リポジトリ KURENAI 紅 Kyoto University Research Information Repository

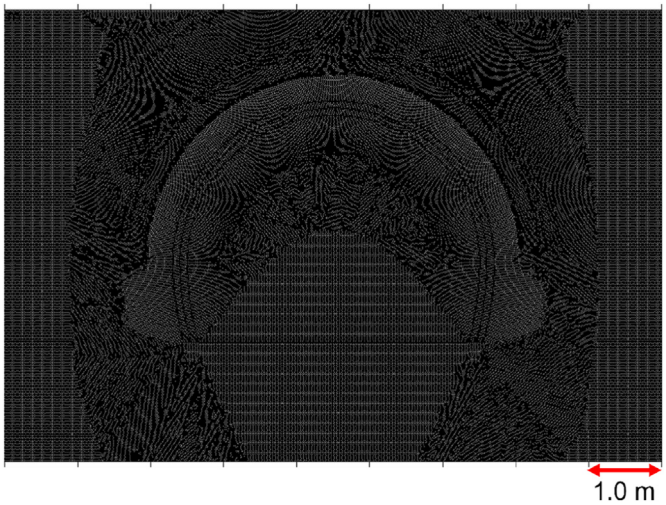

Fig. 5. Enlarged view of finite elements in the niche and surrounding area.

MPa) and vertical stress (5.61 MPa) measured at 350 m depth, and z is the depth. In addition, body force due to gravity was also applied dependent on the nominal density ρ_t. The distribution of the pore pressure within the numerical domain was obtained by conducting a steady state seepage analysis with the hydraulic gradient of 1/1000 (Japan Nuclear Cycle Development Institute, 2005) before performing the excavation analysis. In this seepage analysis, the initial pore pressure was set to a depth-dependent hydrostatic pressure distribution, and the total water heads at the left and right boundaries of the numerical domain were set to 375 m and 375 + 0.001 × 85 m, respectively to simulate hydraulic gradient of 1/1000.

In the implementation of the excavation analysis, firstly, the internal outward radial stress applied to the boundary of the niche to replace the in-situ stress components (i.e., equivalent excavation stress) was obtained from by a self-weight analysis and then released monotonically 0.1% per step. In addition, based on the actual excavation process, which was the same as that in Aoyagi and Ishii (2018), the current analysis assumed the excavation at the representative section within the area where support structures, excluding the rockbolts, were installed with every 1.5-m advancement of the excavation face. Thus, only the installation of the 200-mm-thick shotcrete and steel arch ribs, shown in Fig. 4, was considered in the analysis. According to a previous report by Morioka et al. (2008), the 1.5-m advancement of the excavation face corresponds to a stress release rate of approximately 78% for the case of $d =$ 4.0 m; and thus, the aforementioned support structures were installed at the end of analysis step 780 (stress release rate of 78%), and then 100% of the equivalent excavation stress was released. Solid elements and beam elements were used for the shotcrete and steel arch ribs, respectively (Aoyagi and Ishii, 2018). It should be noted that, in order to ensure the convergence of the computation, the fracture initiation and propagation were determined separately after the stress/deformation analysis in only one stage of the final completion of the excavation immediately after the installation of the supporting structures, while they were determined simultaneously in all other stages of the excavation.

Furthermore, this excavation analysis assumed a short excavation period in a rock mass, and pore pressure dissipation during the excavation was not taken into account. Therefore, in the setting where the undrained condition was assumed at the boundary of the niche, a mechanical calculation alone was performed instead of a coupled mechanical-seepage calculation, and the effective stresses were calculated using the initial pore pressure.

The parameters for the target rock used in the analysis are listed in Table 1. It should be noted that, among these parameters, the calibrated parameters are the residual strength constant η (see Eq. (7)), the characteristic values for the distributions of the uniaxial tensile strength and uniaxial compressive strength by the Weibull distribution (f_{t0}^s and f_{c0}^s, see Eq. (9)), and the homogeneity index m of the Weibull distribution (see Eq. (9)). All the other parameters in Table 1 are set to have values that were measured in previous experimental studies (Aoyagi and Ishii, 2018; Miyazawa et al., 2011). For example, in terms of the non-calibrated mechanical parameters in this table, their values were set to have the average values of the mechanical properties obtained from laboratory experiments on rock cores extracted from a borehole drilled in the 350-m gallery of the Honorobe URL (Aoyagi and Ishii, 2018). On the other hand, for the parameters that required calibration, the appropriate values were identified after referring to the literature (Zhu and Tang, 2004; Liu et al., 2004; Li et al., 2013; Li and Tang, 2015) and through a trial-and-error process, reproducing the actual EDZ characteristics adequately. For example, the characteristic values for the distributions of uniaxial tensile strength and uniaxial compressive strength by the Weibull distribution ($f_{t0}{}^s$and $f_{t0}{}^s$) were calibrated to be slightly larger than the aforementioned average values (Aoyagi and Ishii, 2018). This is because the previous studies (Zhu and Tang, 2004; Li et al., 2013; Li and Tang, 2015) confirmed that, in order to reproduce the actual durability of rocks, it is necessary to set the characteristic values of the uniaxial tensile strength and uniaxial compressive strength at higher values than the experimental ones when performing the mechanical calculation, including fracture generation, by incorporating the heterogeneity of the rocks. In addition, homogeneity index m was set to be 4.0 based on previous works (Zhu and Tang, 2004; Liu et al., 2004), which suggested the appropriate range of m (1.2–5.0) for realistically capturing the fracturing behavior of rocks. Regarding the mechanical properties of the shotcrete and steel arch ribs, the values in Table 2 were set uniformly within the relevant area based on the standard specifications of concrete materials (JapanSociety of Civil Engineers, 2002) and those of the steel arch ribs from the Japanese Chronological Scientific Tables (National Astronomical Observatory, 2005).

Table 1
Parameters for rock used in simulation.

Parameter	Value
Residual strength constant [−] η	0.2* (Calibrated)
Homogeneity index of material properties [−] m	4.0 (Zhu and Tang, 2004; Liu et al., 2004)
Characteristic value of elastic modulus [GPa] $E_0{}^s$	1.82 (Aoyagi and Ishii, 2018)
Characteristic value of uniaxial tensile strength [MPa] $f_{t0}{}^s$	1.83 (Aoyagi and Ishii, 2018) × 2.5* (Calibrated)
Characteristic value of uniaxial compressive strength [MPa] $f_{c0}{}^s$	15.4 (Aoyagi and Ishii, 2018) × 2.5* (Calibrated)
Internal friction angle [°] θ	24.5 (Aoyagi et al., 2015)
Poisson's ratio [−] ν	0.17 (Aoyagi and Ishii, 2018)
Biot-Willis coefficient [−] α_B	0.92 (Miyazawa et al., 2011)

*The values are determined by calibration.

3.2. Comparison with characteristics of EDZ obtained from in-situ tests

Different snapshots of the distribution of damage variable D around the niche during the excavation are depicted in Fig. 6. The figure shows that fracture zones (i.e., areas where damaged elements coalesce) had

Table 2
Parameters for shotcrete and steel arch ribs used in simulation.

Parameter	Shotcrete	Steel arch rib
Elastic modulus [GPa]	20 [a]	210 [b]
Poisson's ratio [−]	0.2 [a]	0.3 [b]
Cross-sectional area [m^2]	0.92 [a]	4.72×10^{-3} [b]
Moment inertia [m^4]	–	2.0×10^{-5} [b]
Density [kg m^{-3}]	3150 [a]	–

[a] Values determined by the JapanSociety of Civil Engineers (2002)
[b] Values determined by the National Astronomical Observatory (2005)

京都大学 KYOTO UNIVERSITY
A Self-archived copy in
Kyoto University Research Information Repository
https://repository.kulib.kyoto-u.ac.jp
京都大学学術情報リポジトリ KURENAI 紅 Kyoto University Research Information Repository

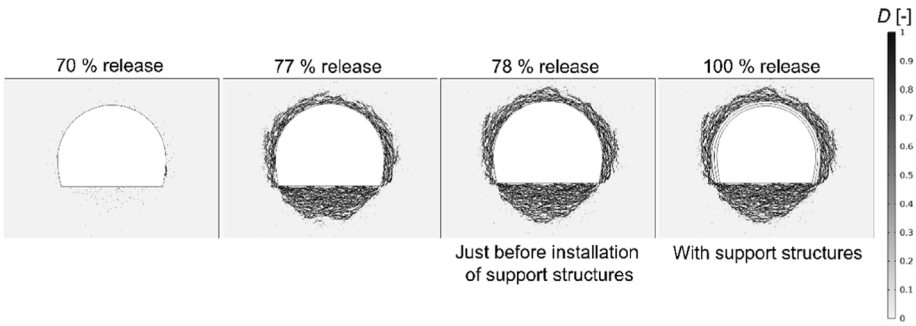

Fig. 6. Simulated evolution of damaged zone at stress release rates of 70%, 77%, 78%, and 100% during excavation of Niche No. 3.

already developed around the niche prior to the installation of the support structures (i.e., after 78% of the equivalent excavation stress had been released), and that after the installation of the structure supports, the distribution of fracture zones became somewhat denser around the unsupported floor area of the niche.

At the end of the excavation analysis, the extent of the EDZ, was examined. In the in-situ excavation, the fractures distribution on sidewall and below the floor of Niche No. 3 using BTV surveys of boreholes, and the dense fracture zone was observed up to 0.6 m for the sidewalls and 1.6 m below the floor as the region of the EDZ (Aoyagi and Ishii, 2018). Details on the above-mentioned in-situ observations can be found in the literature (Aoyagi and Ishii, 2018). In the current excavation analysis using the continuous damage model, the dense fracture zone can be approximated as the region where many damaged elements (i.e., cracked elements) coalesce. Thus, as the maximum extent of the simulated EDZ, maximum extent of the area where the damaged elements are continuously connected from the cavity boundary was extracted. As a result, the maximum extent of simulated EDZ is approximately 0.68 m for the sidewall, and 1.65 m below the floor (see Fig. 7). Since this result is very close to the in-situ observations described above, it can be confirmed that the applied numerical analysis is adequately calibrated to capture the actual trend in the EDZ expansion at the target site. It is noted that the numerical analysis in the present study more accurately reproduced the actual area of the EDZ compared to the extent of the EDZ (the sidewall: 0.9 m and below the floor: 1.3 m) obtained by the only previous study (Aoyagi and Ishii, 2018) that attempted to numerically reproduce the EDZ generated in the same excavation test as the target of this chapter.

Furthermore, the trend in failure modes for the EDZ was also investigated, as shown in Fig. 8. This figure depicts the failure modes of the distributed damaged zones around the niche at the end of the excavation analysis. It is apparent from the figure that, although the hybrid damaged region induced by both tension and shear is the most dominant, a number of damaged elements induced by tension only can also be observed and more frequently than those induced by shear only around the niche. This tendency ought to be harmonious with the suggestion from the in-situ observations using the rock cores from boreholes that the hybrid and tensile fractures constitute the EDZ (Aoyagi and Ishii, 2018). In addition, regarding the direction of the fracture growth, it can be seen that most of the fracture zones form parallel to the niche wall. This should be attributed to the predominant tensile deformation between the niche wall and the surrounding area due to the displacements in the direction of the decreasing internal space of the niche, as shown in Fig. 9.

Moreover, in order to further investigate the process of the EDZ development in greater detail, the changes in the total area of the damaged zone ($D > 0$) within the numerical domain, along with the progress of the excavation, are shown in Fig. 10. The figure shows the behavior whereby the total damaged zone developed rapidly after the stress release rate reached about 74%, and eventually increased to about

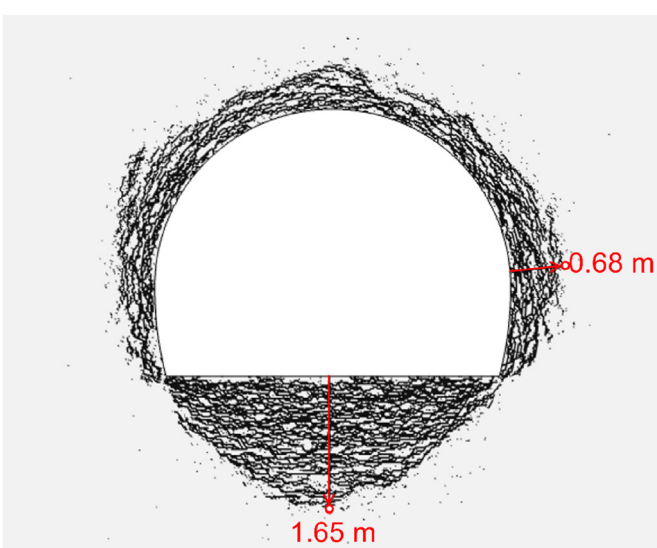

Fig. 7. Extent of simulated EDZ around Niche No. 3 at end of excavation analysis.

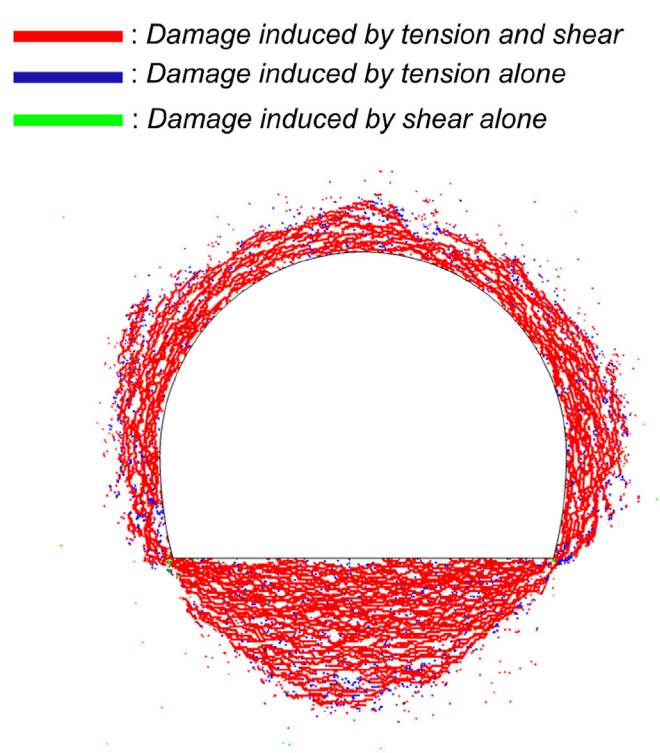

Fig. 8. Distributions of damage modes around Niche No. 3 at end of excavation analysis.

京都大学 KYOTO UNIVERSITY
A Self-archived copy in
Kyoto University Research Information Repository
https://repository.kulib.kyoto-u.ac.jp
京都大学学術情報リポジトリ KURENAI 紅 Kyoto University Research Information Repository

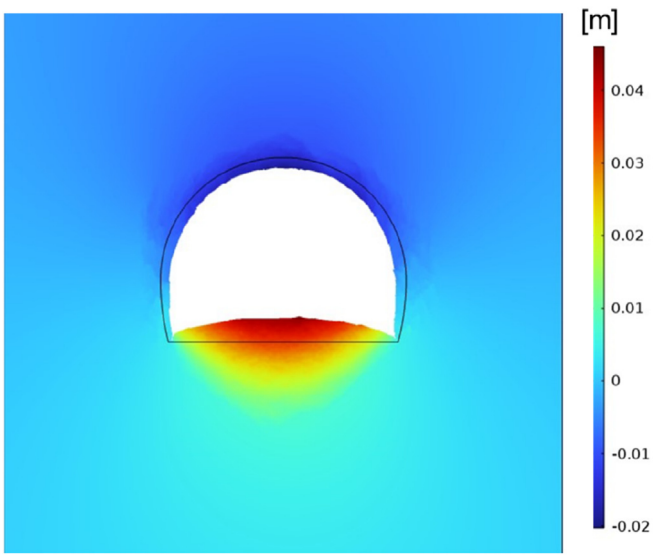

Fig. 9. Distribution of vertical displacement around Niche No. 3 at stress release rate of 78% (Note: The amount of deformation in the figure is magnified 10 times the actual value).

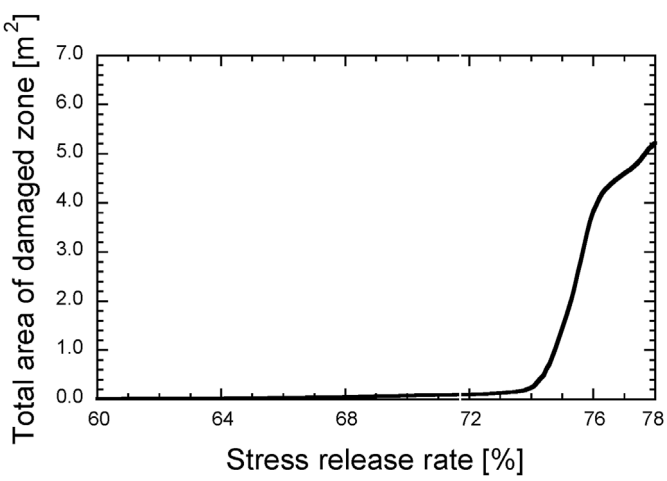

Fig. 10. Variation in total area of damaged zone with stress release rate during excavation of Niche No. 3.

5.2 m^2.

4. Numerical simulations for EDZ development expected in geological disposal of HLW

Through the simulation in Chapter 3, it was confirmed that a calibrated numerical analysis, including the rock fracturing process, can successfully address the actual trends in the EDZ generated in the siliceous mudstone formation examined in one of the representative and important underground research sites in Japan (i.e., the Horonobe URL). In this chapter, a calibrated numerical analysis is used to predict the distribution of the EDZ generation during the excavation of a cavity when implementing the geological disposal of HLW in the same geological environment as in Chapter 3.

The model geometry and boundary conditions used in this analysis are shown in Fig. 11. While most parts of the setting and the implementation of the analysis are the same as in Chapter 3, changes have been made with respect to the excavated cross section and the installation of the support structures. In this analysis, the horizontal storage of HLW was assumed as described in the scientific and technical report summarizing

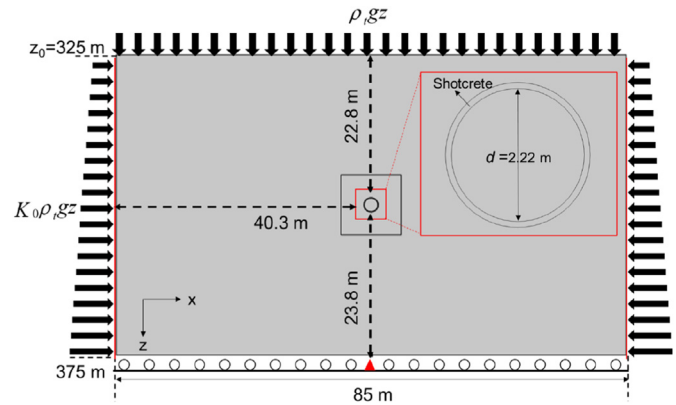

Fig. 11. Description of numerical analysis for simulating excavation of cavity within geological disposal facility of HLW.

the HLW disposal construction in Japan (Japan Nuclear Cycle Development Institute, 2000). According to the report (Japan Nuclear Cycle Development Institute, 2000), when geological disposal is conducted in the case of horizontal storage, only shotcrete is installed as the support structure for every 1.0-m advancement of the excavation face. The prescribed diameter d of the cavity was 2.22 m and, based on the relationship between the tunnel face distance and the stress release rate, reported in Morioka et al. (2008), the 1.0-m advancement of the excavation face corresponds to a stress release rate of approximately 76%. In the analysis, therefore, the shotcrete was installed at the end of analysis step 760 (stress release rate of 76%), and then 100% of the equivalent excavation stress was released. All the parameters selected for the analysis, as well as the determined values, are given in Tables 1 and 2. The numerical domain was discretized into 531536 rectangular elements. As well as the numerical analysis presented in Chapter3, in the 10-m-square area around the cavity, the average mesh size was set to about 0.02 m, much finer than in other areas.

The simulated results for the evolving distribution of the fractures (i.e., the evolution of the distribution of damage variable D) generated around the cavity during the excavation are shown in Fig. 12. The figure shows that fracture zones were generated around the periphery of the cavity before the installation of the shotcrete, and that almost no new fracture zones occurred at all after the introduction of the shotcrete. The distribution of generated cracks was relatively uniform around the cavity. This is because the target cross section of the tunnel is not such that intensive deformation acts on one part of the tunnel, as seen as in Fig. 9, under confining pressures with small anisotropy ($K_0 = 0.98$). With respect to the damage modes of the fractures, the hybrid-type damage, induced by both tension and shear, is the most dominant, followed by the type of damage promoted only by tension (see Fig. 13). It should be noted that the maximum extent of the dense fracture zone with the same definition as described in Chapter3 at the end of the excavation analysis was about 0.35 m from the cavity wall (see Fig. 14). In addition, to further quantify the evolutionary behavior of the EDZ expansion, the relation between the total area of the damaged zone within the analysis domain and the stress release rate during the excavation process, is depicted in Fig. 15. From the figure, it can be confirmed that after the stress release rate of approximately 73% (i.e., about 3.0% before the stress release rate of 76% during the shotcrete placement), the total area of the damaged zone increased significantly and finally reached about 1.1 m^2. Incidentally, the predicted total damaged area was approximately 0.28 times the area of the tunnel cross section.

5. Conclusion

The aim of the present study was to realize a realistic numerical analysis considering the nucleation and growth of rock fractures, which

京都大学 KYOTO UNIVERSITY
A Self-archived copy in
Kyoto University Research Information Repository
https://repository.kulib.kyoto-u.ac.jp
京都大学学術情報リポジトリ KURENAI 紅 Kyoto University Research Information Repository

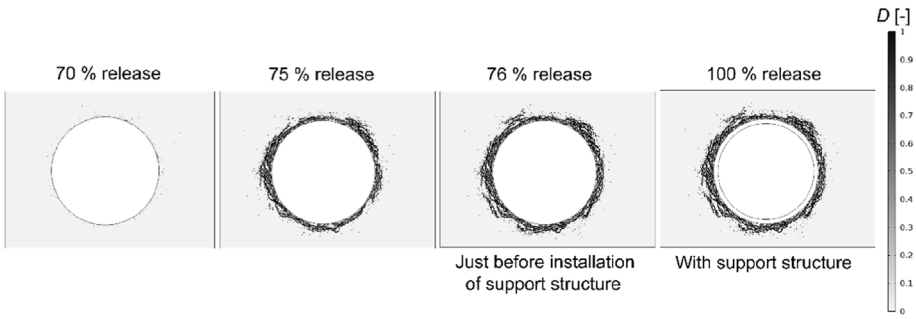

Fig. 12. Simulated evolution of damaged zone around cavity at stress release rates of 70%, 75%, 76%, and 100% during excavation within geological disposal facility of HLW.

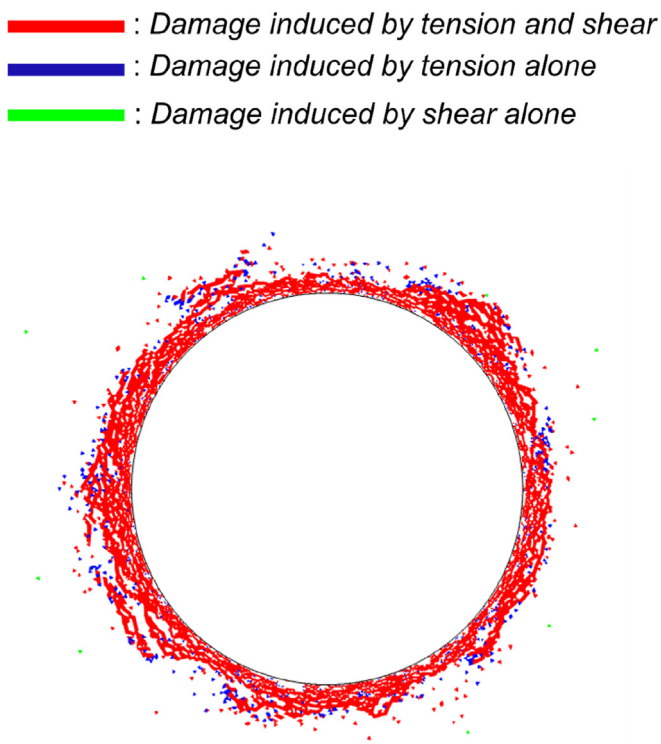

Fig. 13. Distributions of damage modes around cavity at end of analysis for cavity excavation within geological disposal facility of HLW.

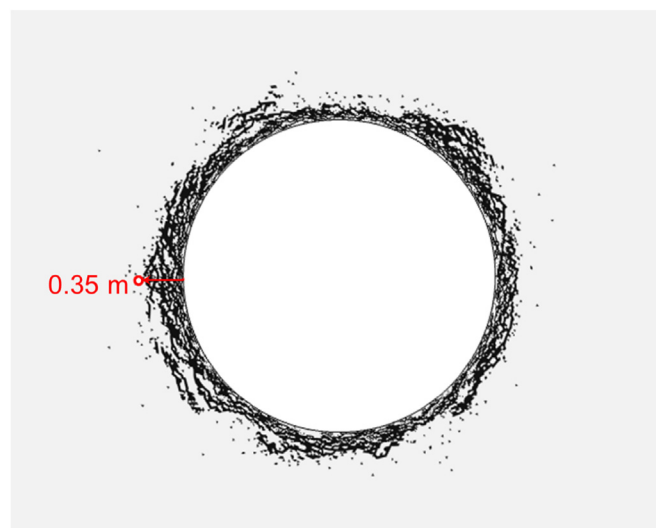

Fig. 14. Extent of simulated EDZ around cavity at end of analysis for cavity excavation within geological disposal facility of HLW.

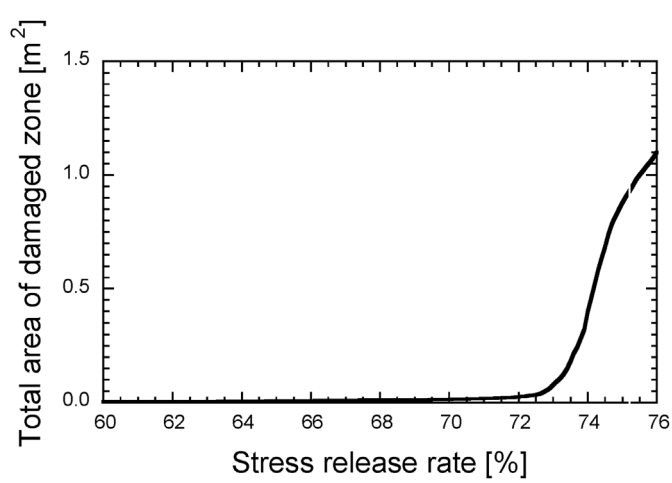

Fig. 15. Variation in total area of damaged zone with stress release rate during cavity excavation within geological disposal facility of HLW.

can accurately replicate the trends in the EDZ observed from one of the representative and important underground research fields in Japan, Horonobe URL, where very limited attempts have been made to simulate the EDZ distribution. Firstly, a FEM-based numerical analysis employing a damage model, which is capable of solving both rock deformation and rock fracturing simultaneously, was proposed. Secondly, the proposed analysis was applied to replicate the niche excavation in the gallery of the Horonobe URL, at a depth of 350 m, and calibrated through comparisons with the in-situ observations of the EDZ distribution in a mudstone formation (extent of the EDZ and failure modes of the generated fractures). From the comparisons, it was confirmed that the simulated results not only agreed well with the measured results for the EDZ, in terms of the extent, but were also able to capture the realistic failure modes of the fractures constituting the EDZ suggested from the in-situ observations. Consequently, this simulation provided the confidence that the authors have succeeded in establishing an appropriately calibrated numerical analysis which precisely replicates the actual trends in the EDZ generated at the targeted site. Finally, assuming the implementation of the geological disposal of HLW at the same site (i.e., at a depth of 350 m in the Horonobe URL), a numerical experiment was conducted to predict the EDZ distribution by applying a calibrated numerical analysis. The predicted results showed that, under the geological environment assumed in this study, the EDZ dominantly formed by the tensile-shear hybrid fractures rapidly extended about 3.0% prior to the stress release rate when support structures were inserted and eventually rose to

京都大学 KYOTO UNIVERSITY
A Self-archived copy in
Kyoto University Research Information Repository
https://repository.kulib.kyoto-u.ac.jp
京都大学学術情報リポジトリ KURENAI 紅 Kyoto University Research Information Repository

roughly 0.3 m from the cavity wall during the excavation of the disposal cavity for the HLW. Such predicted results, using a model that has already been calibrated by reproducing the in-situ excavation test in the target field, should be useful for understanding and accurately evaluating the development process of the EDZ distribution at that field or in similar environments, and for taking countermeasures against it.

In other words, considering that sedimentary rocks, such as the mudstone, account for a large proportion of the deep underground geological environment in Japan, the present case study on the Horonobe URL, where mudstone is distributed, is an important achievement with high versatility for investigating the performance of natural barriers in the implementation of projects for the geological disposal of HLW in Japan.

Declaration of competing interest

The authors declare that they have no known competing financial interests or personal relationships that could have appeared to influence the work reported in this paper.

Acknowledgements

This work was supported by the JST FOREST Program (Grant no. JPMJFR216Y, Japan) and JSPS KAKENHI (Grant nos. 20K14826, 22H01589, and 22H00229). Their support is gratefully acknowledged. The authors thank Dr. Kazuhei Aoyagi for his advice and discussion on the EDZ generation at the Horonobe URL.

References

Aoyagi, K., Ishii, E., 2018. A method for estimating the highest potential hydraulic conductivity in the excavation damaged zone in mudstone. Rock Mech. Rock Eng. 52, 385–401.
Aoyagi, K., Tsusaka, K., Tokiwa, T., Kondo, K., Inagaki, D., Kato, H., 2013. A study of the regional stress and the stress state in the galleries of the Horonobe Underground Research Laboratory. In: Proceedings of the 6th International Symposium on In-Situ Rock Stress. Sendai. Japan, pp. 331–338.
Aoyagi, K., Ishii, E., Kondo, K., Tsusaka, K., Fujita, T., 2015. A study on the strength properties of the rock mass based on triaxial tests conducted at the Horonobe underground research laboratory. JAEA Res. 2015-001.
Blümling, P., Bernier, F., Lebon, P., Martin Martin, C.D., 2007. The excavation damaged zone in clay formations time-dependent behaviour and influence on performance assessment. Phys. Chem. Earth 32, 588–599.
COMSOL, 2021. COMSOL MULTIPHYSICS. Version 6.0, Documentation. COMSOL AB, Stockholm, Sweden.
Fukuda, D., Mohammadnejad, M., Liu, H., Dehkhoda, S., Chan, A., Cho, S.H., Min, G.J., Han, H., Kodama, J., Fujii, Y., 2019. Development of a GPGPU-parallelized hybrid finite-discrete element method for modeling rock fracture. Int. J. Numer. Anal. Methods GeoMech. 43, 1797–1824.
Giger, S.B., Marschall, P., Lanyon, G.W., Martin, C.D., 2015. Transferring the geomechanical behavior of Opalinus Clay observed in lab tests and Mont Terri URL to assess engineering feasibility at potential repository sites. In: 49th US Rock Mechanics/Geomechanics 704 Symposium 2015, vol. 3. American Rock Mechanics Association (ARMA), pp. 2384–2391.
Hajiabdolmajid, V., Kaiser, P.K., Martin, C.D., 2002. Modeling brittle failure of rock. Int. J. Rock Mech. Min. Sci. 59, 731–741.
Jia, P., Yang, T.H., Yu, Q.L., 2012. Mechanism of parallel fractures around deep underground excavations. Theor. Appl. Fract. Mech. 61, 57–65.
Japan Nuclear Cycle Development Institute, 2005. Development and Management of the Technical Knowledge Base for the Geological Disposal of HLW, Summary of the H17 Project Reports, 1. Scientific Research of Deep Underground. JNC TN1400 2005-014.
Japan Society of Civil Engineers, 2002. Standard Specifications for Concrete Structures-2002, Materials and Construction. JSCE Guidelines for Concrete, Maruzen.
Japan Nuclear Cycle Development Institute, 2000. 2000: Second Progress Report on Research and Development for the Geological Disposal of HLW in Japan, Supporting Report 2 Repository Design and Engineering Technology, H12: Project to Establish the Scientific and Technical Basis for HLW Disposal in Japan. JNC TN1410 2000-003, IV-139-IV-160.
Kelsall, P.C., Case, J.B., Chabanne, C.R., 1984. Evaluation of excavation induced changes in permeability. Int. J. Rock Mech. Min. Sci. 21, 121–135.
Li, G., Tang, C.A., 2015. A statistical meso-damage mechanical method for modeling trans-scale progressive failure process of rock. Int. J. Rock Mech. Min. Sci. 74, 133–150.
Li, L.C., Liu, H.H., 2013. A numerical study of the mechanical response to excavation and ventilation around tunnels in clay rocks. Int. J. Rock Mech. Min. Sci. 59, 22–32.
Li, L.C., Tang, C.A., Wang, S.Y., Yu, J., 2013. A coupled thermo-hydrologic-mechanical damage model and associated application in a stability analysis on a rock pillar. Tunn. Undergr. Space Technol. 34, 38–53.
Liu, H.Y., Roquete, M., Kou, S.Q., Lindqvist, P.A., 2004. Characterization of rock heterogeneity and numerical verification. Eng. Geol. 72, 89–119.
Marschall, P., Giger, S., Vassiere, D.L.R., Shao, H., Leung, H., Nussbaum, C., Trick, T., Lanyon, B., Senger, R., Lisjak, A., Alcolea, A., 2017. Hydro-mechanical evolution of the EDZ as transport path for radionuclides and gas: insights from the Mont Terri rock laboratory (Switzerland). Swiss J. Geosci. 110, 173–194.
Morioka, H., Yamazaki, M., Matsui, H., Orukawa, G., Yamaguchi, T., 2008. Support design of underground facilities in the Horonobe underground research laboratory project. JAEA Res. 2008-009, 1–263.
Miyazawa, D., Sanada, H., Kiyama, T., Sugita, Y., Ishijima, Y., 2011. Proelastic coefficients for siliceous rocks distributed in the Horonobe area, Hokkaido, Japan. J. MMIJ 127, 132–138.
National Astronomical Observatory, 2005. Chronological Scientific Tables 2005. Maruzen, Tokyo.
Ogata, S., Yasuhara, H., Kinoshita, N., Kishida, Kiyoshi, 2020. Coupled thermal–hydraulic–mechanical–chemical modeling for permeability evolution of rocks through fracture generation and subsequent sealing. Comput Geosci. 24, 1845–1864.
Ota, K., Abe, H., Yamaguchi, T., Kunimaru, T., Ishii, E., Kurikami, H., Tomura, G., Shibano, K., Hama, K., Matsui, H., Niizato, T., Takahashi, K., Niunoya, S., Ohara, H., Asamori, K., Morioka, H., Funaki, H., Shigeta, N., Fukushima, T., 2007. Horonobe underground research laboratory project synthesis of phase I investigations 2001-2005 volume "geoscientific research. JAEA Res. 2007-044, 1–434.
Souley, M., Homand, F., Peda, S., Hoxha, D., 2001. Damaged-induced permeability changes in granite: a case example at the URL in Canada. Int. J. Rock Mech. Min. Sci. 38, 297–310.
Saegusa, H., Seno, Y., Nakama, S., Tsuruta, T., Iwatsuki, T., Amano, K., Takeuchi, R., Matsuoka, T., Onoe, H., Mizuno, T., Oyama, T., Hama, K., Sato, T., Kuji, M., Kuroda, H., Semba, T., Uchida, M., Sugihara, K., Sakamaki, M., 2007. Final report on the surface-based investigation (phase I) at the Mizunami Underground Laboratory project. JAEA Res. 2007-043, 1–337.
Smith, G.M., Young, L.E., 1955. Ultimate theory in flexure by exponential function. J. ACI 52, 349–359.
Tomita, A., Tasaka, Y., Ohmori, T., Oka, F., Adachi, T., 2010. An elasto-viscoplastic hydro-mechanical coupled analysis and its application to a cavern excavation in soft rocks. Doboku Gakkai Ronbunshuu C. 66, 202–214.
Tsang, C.-F., Jing, L., Stephansson, O., Kautsky, F., 2005. The DECOVALEX III project: a summary of activities and-lessons learned. Int. J. Rock Mech. Min. Sci. 42, 593–610.
Tamura, T., Adachi, T., 2002. On the domain allocation of finite element method for tunnel excavation, 701/III-58 J. Jpn. Soc. Civ. Eng. 231–242.
Tang, C.A., 1997. Numerical simulation on progressive failure leading to collapse and associated seismicity. Int. J. Rock Mech. Min. Sci. 34, 249–262.
Vlachopoulos, N., Vazaios, I., 2018. The numerical simulation of hard rocks for tunneling purposes at great depths: a compaction between the hybrid FDEM method and continuous techniques. Adv. Civ. Eng. 1–18. Article ID 3868716.
Wang, Y., Liu, Z., Yang, H., Shao, Z., Zhang, Z., 2016. FE analysis of rock with hydraulic-mechanical coupling based on continuum damage evolution. Math. Probl Eng 26, 8534965.
Weibull, W., 1951. A statistical distribution function of wade applicability. J. Appl. Mech. 18, 293–297.
Zhang, C.-H., 2016. The stress-strain-permeability behaviour of clay rock during damage and recompaction. J. Rock Mech. Geotech. Eng. 8, 16–26.
Zhu, W.C., Tang, C.A., 2004. Micromechanical model for simulating the fracture process of rock. Rock Mech. Rock Eng. 37, 25–56.